ADVANCED ENERGY MATERIALS
www.advenergymat.de

Phase Boundary Mapping of Tin-Doped ZnSb Reveals Thermodynamic Route to High Thermoelectric Efficiency

*Maxwell Wood, Michael Y. Toriyama, Shristi Dugar, James Male, Shashwat Anand, Vladan Stevanović, and G. Jeffrey Snyder**

The thermoelectric material ZnSb utilizes elements that are inexpensive, abundant, and viable for mass production. While a high thermoelectric figure of merit zT, is difficult to achieve in Sn-doped ZnSb, it is shown that this obstacle is primarily due to shortcomings in reaching high enough carrier concentrations. Sn-doped samples prepared in different equilibrium phase spaces in the ternary Zn-Sb-Sn system are investigated using phase boundary mapping, and a range of achievable carrier concentrations is found in the doped samples. The sample with the highest zT in this study, which is obtained with a carrier concentration of 2×10^{19} cm^{-3} when the material is in equilibrium with Zn_4Sb_3 and Sn, confirms that the doping efficiency can be controlled by preparing the doped sample in a particular region of the thermodynamic phase diagram. Moreover, density functional theory calculations suggest that the doping efficiency is limited by the solubility of Sn in ZnSb, as opposed to compensation from native defects. Cognizance of thermodynamic conditions is therefore crucial for rationally tuning the carrier concentration, a quantity that is significant for many areas of semiconductor technologies.

1. Introduction

Thermoelectric materials allow for the conversion of heat into electricity completely in the solid state.[1] This enables reliable deep space missions and remote power sources which have inspired uses for a variety of waste heat converters in automobiles and consumer products. However, the cost and environmental hazard of constituent elements in many efficient thermoelectric materials, such as toxic lead in PbTe, can limit the use of thermoelectric materials. This concern has driven the discovery and development of new thermoelectric materials with less expensive and more environmentally friendly elements. Zn, Sb, and Sn are inexpensive, relatively non-toxic, and sufficiently abundant elements to be viable for commercial applications.[2] The efficient use of thermoelectric materials depends upon its dimensionless figure of merit, zT:

$$zT = \frac{\alpha^2 \sigma T}{\kappa} \tag{1}$$

where α is the Seebeck coefficient, σ is the electrical conductivity, κ is the total thermal conductivity, and T is the absolute temperature.

ZnSb has been studied extensively for use as a thermoelectric material, because it possesses many characteristics commonly found in good thermoelectric materials.[2] Zn and Sb have similar electronegativities for covalent bonding, which enable favorable electrical transport properties, but the relatively large Sb enables soft bonding needed for low thermal conductivity. ZnSb contains the Zintl anion complex Sb_2^{4-}, which adds further structural complexity contributing to the low thermal conductivity (**Figure 1**). The Zintl valence balance explains why ZnSb is a small band gap semiconductor like most good thermoelectric materials.[3]

The main challenge for ZnSb thermoelectrics has been to achieve $zT > 0.6$ consistently.[2,4] The suboptimal figure of merit is due to shortcomings in achieving high enough carrier concentrations, as evidenced by the single parabolic band model;[5] while the optimal carrier concentration for ZnSb is 1.8×10^{19} cm^{-3} corresponding to a zT of 0.75 at 700 K,[5] many doped ZnSb samples with lower zT have reported Hall carrier concentrations significantly less than that value.[6,7]

There are several possible reasons for suboptimal carrier concentrations in doped semiconductors. A low doping efficiency, or concentration of charge carriers generated per dopant atom, may be attributed to native defects (vacancies, interstitials, and antisites). Often in doped samples that exhibit low carrier concentrations, a native defect either partially or fully compensates the added charge of the dopant.[8] The maximum attainable carrier concentration, or dopability,[9] could also be limited by the solubility of the dopant in the material. This occurs in

Dr. M. Wood, M. Y. Toriyama, S. Dugar, J. Male, Dr. S. Anand, Prof. G. J. Snyder
Northwestern University
Evanston, IL 60208, USA
E-mail: jeff.snyder@northwestern.edu
Dr. M. Wood
Jet Propulsion Laboratory
California Institute of Technology
Pasadena, CA 91109, USA
Prof. V. Stevanović
Colorado School of Mines
Golden, CO 80401, USA
The ORCID identification number(s) for the author(s) of this article can be found under https://doi.org/10.1002/aenm.202100181.

DOI: 10.1002/aenm.202100181

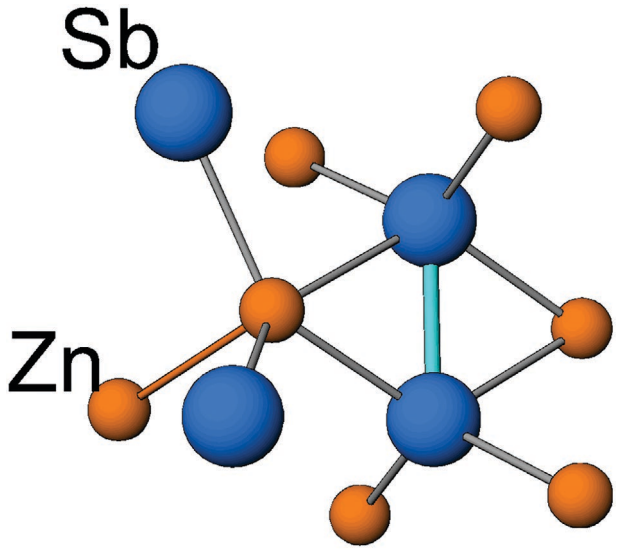

Figure 1. Structure of ZnSb highlighting the Sb–Sb dimer.

cases where adding a high concentration of the dopant species induces phase segregation instead of fully incorporating in the material. Accordingly, a rational explanation for disparities in the reported zT values of ZnSb with the same dopant is that the thermodynamic conditions involved are different. Samples with seemingly similar chemical compositions but prepared in slightly different ways can be in equilibrium with different competing phases, which can drastically alter the dopant solubility or native defect concentrations. For example, it was thought for many years that Yb and Ce had limited solubility in skutterudite $CoSb_3$; however, by changing the equilibrium thermodynamic conditions, the solubility of these rare earth dopants was doubled.[10]

The full range of thermodynamically accessible dopabilities can be explored experimentally using phase boundary mapping.[11–13] For Sn-doped ZnSb, this means investigating the phase spaces of the isothermal Zn–Sn–Sb ternary phase diagram around ZnSb. In this procedure, the different thermodynamic states of ZnSb, defined by the accessible range of chemical potentials, can be explored by testing samples in all distinct three-phase equilibria. Such a method effectively probes the full range of thermodynamically accessible defect concentrations to achieve the optimal carrier concentration.

Here we show that a higher carrier concentration indeed corresponds to higher zT values. We show that four distinct flavors of Sn-doped ZnSb can be prepared by phase boundary mapping. One of the four samples, synthesized under the most Zn-rich conditions, has a hole carrier concentration over three times higher than those prepared in the other three regions. In concert with density functional theory (DFT) calculations, we show that the hole concentration is limited by the Sn solubility in ZnSb rather than a compensating native defect. This provides a thermodynamic explanation for the conflicting reported properties and zT of the same nominal composition and provides a rational synthesis route to consistently achieve high zT thermoelectric materials.

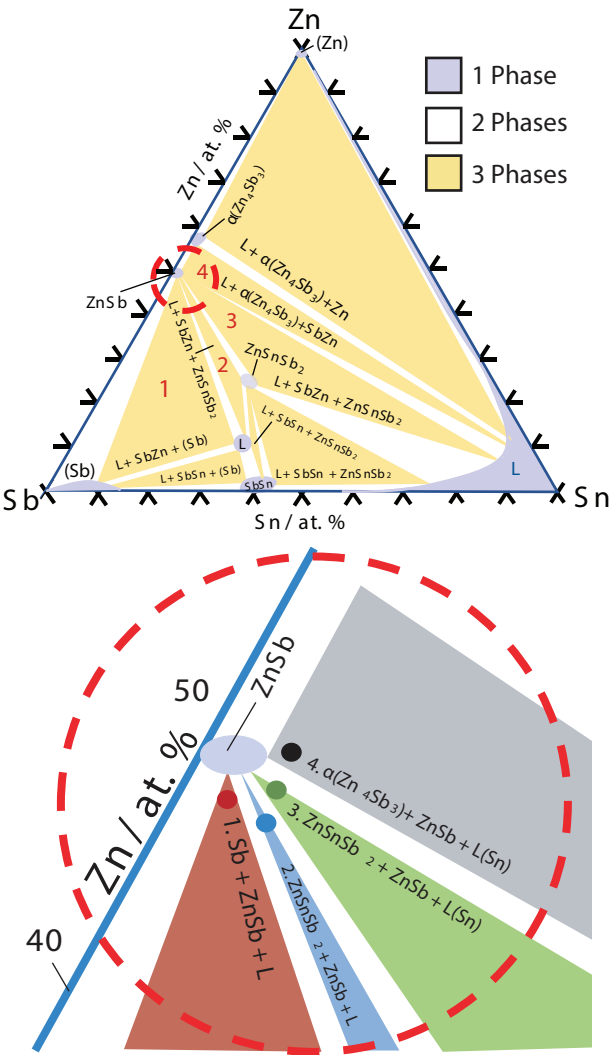

Figure 2. a) The Zn–Sb–Sn equilibrium phase diagram at 400 °C, as identified by Wang et. al.[14] Lavender areas represent single-phase regions, white regions are two-phase regions, and yellow regions are three-phase regions. b) The phase diagram zoomed into the ZnSb composition shows four distinct three-phase regions accessible by doping ZnSb with Sn. The defect concentrations, and subsequently the charge carrier concentrations, in ZnSb will be different in each region. The compositions of the four samples presented in this study are indicated by the four points in the phase diagram and tabulated in Table 1.

2. Experimental Results

2.1. Phase Identification

Four three-phase regions have been identified around ZnSb at 400 °C by Wang et al.[14] (**Figure 2**). Each of the four phase spaces are identified by both XRD and electron microscopy. Small impurity peaks are identified in the XRD patterns (**Figure 3**), corresponding to the impurity phases expected from the equilibrium phase diagram. Electron microscopy clearly shows two distinct impurity phases in each sample along with the majority ZnSb phase (**Figure 4**). The approximate compositions of the impurity phases are measured by combined EDS

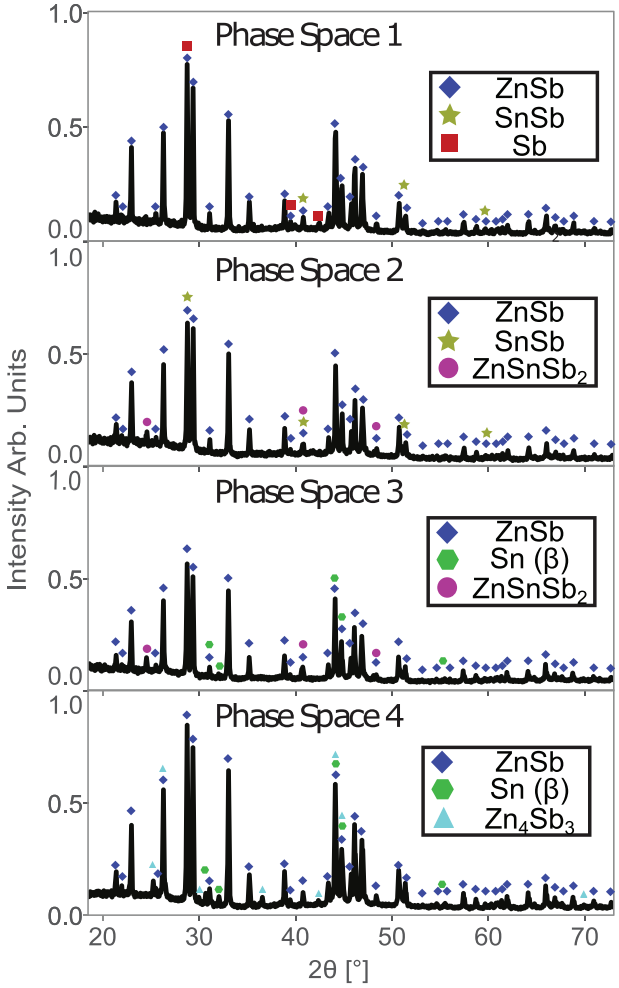

Figure 3. X-ray diffraction patterns of samples in each of the four phase spaces around ZnSb designated in Figure 2. In each sample, ZnSb is present along with two secondary phases commensurate with the phase diagram.

and WDS quantitative analysis (**Table 1**), and they fall within 1% of the composition expected from the equilibrium phase diagram. The impurity phase Zn_4Sb_3 is a well-known p-type thermoelectric phase,[15,16] while $ZnSnSb_2$ has only a small window of stability.[17] The two different liquid phases that appear in the 400 °C phase diagram transform primarily into crystalline Sn and SnSb when quenched to room temperature.

2.2. Thermoelectric Properties

Thermoelectric transport properties of Sn-doped ZnSb prepared in the different phase spaces vary considerably. The Hall carrier concentration (n_H) of the sample in phase space 4 is significantly higher than that of the samples in phase spaces 1, 2, and 3 (**Figure 5**). Both the electrical resistivity and Seebeck coefficient increase with temperature (**Figure 6**a,b), following the expected trend for a heavily doped semiconductor. The thermal conductivity decreases with temperature (Figure 6c), indicating that scattering due to phonons is the dominant scattering mechanism. The sample in phase space 4 with the highest hole concentration has correspondingly the lowest electrical resistivity and highest thermal conductivity due to the electronic contribution to the thermal conductivity. The sample prepared in phase space 4 also exhibits the lowest Seebeck coefficient, which is expected from the large carrier concentration.

During heating and cooling, there is noticeable hysteresis in many of the measured properties. The hysteresis may be due to cracking, electrical contacts, or fluctuating solubilities of the constituent elements. It is known that Zn is mobile in compounds that contain Zn and Sb, even at room temperature.[18]

3. Discussion

The culprit for the disparate zT previously reported in Sn-doped ZnSb is likely the thermodynamic synthesis conditions and the ensuing carrier concentration. We predict the optimum carrier concentration for ZnSb to be 1.8×10^{19} cm^{-3} by assuming electronic transport from a single parabolic band with effective mass $m^* = 0.6m_e$ and electron scattering dominated by acoustic phonons[19] (**Figure 7**a). We find that the Sn-doped ZnSb sample prepared in phase space 4 achieves a near-optimum hole concentration, corresponding to high zT reports of Shabaldin et al.[20] and Valset et al.[7] Our results therefore suggest that the samples in those studies with successfully high carrier concentration were synthesized under equilibrium conditions similar to those set in phase space 4 of this study (Figure 7b). On the other hand, the lower zT observed by Böttger et al.,[5] which was a consequence of lower carrier concentrations, likely had equilibrium conditions similar to phase space 1. Recent reports of high zT by Moghaddam et al., where authors added Zn_4Sb_3 to Ge-doped ZnSb samples also support the conclusion that being in equilibrium with Zn_4Sb_3 allows for an optimal dopability of ZnSb samples. Table 1 compares the 50 °C Seebeck coefficient, which is an indicator of doping level in a material, of different samples from the literature to their peak zT. Samples with high zT have Seebeck values close to what we experimentally find in phase space 4 of this study. One will note the literature generally reports samples with a higher zT than what we find in this study. We attribute this difference to other study's samples generally having a lower thermal conductivity than what we find. This is likely due to other group's work in optimizing the material's microstructure, which was not the focus here.

Knowledge of the samples' equilibrium conditions comes from paying close attention to secondary phases present in each sample and relating them to the Zn–Sb–Sn ternary phase diagram. For instance, a sample with an initial composition having excess Zn (corresponding to a point in phase space 4) may actually become Zn-deficient (corresponding to a point in either phase space 1, 2, or 3) during an annealing step due to the relative ease of sublimation of Zn.[20] It is therefore important to explore the accessible phase spaces of the ternary phase diagram using phase boundary mapping. Within a three-phase region of a three component system at a fixed temperature and pressure, the atomic chemical potentials of the constituent elements (in this case Zn, Sb, and Sn) remain constant. Even slight variations of the nominal composition (e.g., by sublimation) do not affect the atomic chemical potentials, as long as

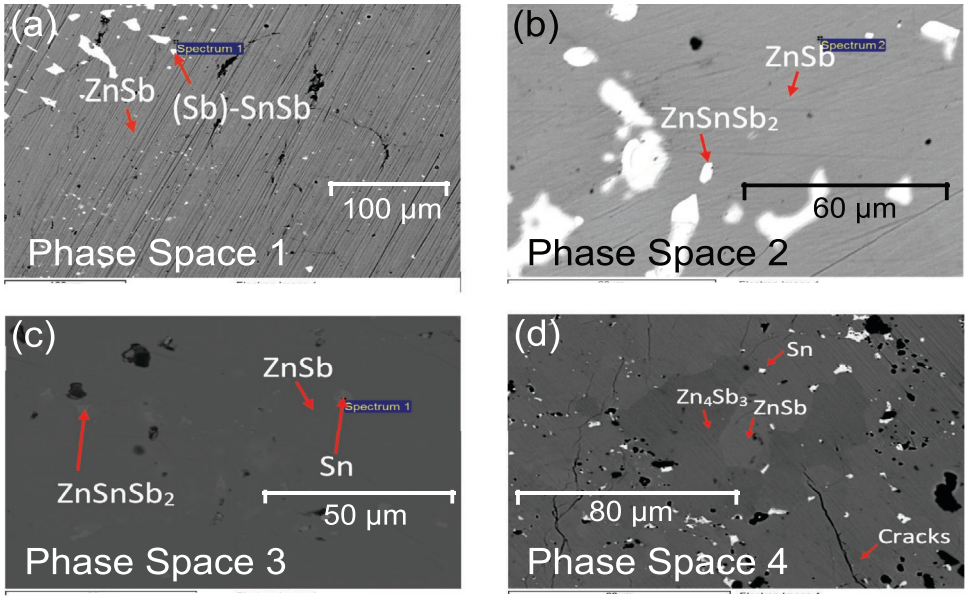

Figure 4. Backscatter SEM images of the four samples prepared in a) phase space 1, b) phase space 2, c) phase space 3, and d) phase space 4 in the Zn–Sb–Sn ternary phase diagram. In each sample, ZnSb is present along with two secondary phases that are identified in the phase diagram.

the compositions reside in the same three-phase region. Consequently, the formation energy of defects is unchanged for all samples prepared in a given three-phase region; conversely, the carrier concentration can be tuned by preparing the sample in the different accessible three-phase regions.

3.1. Defects Controlling the Hole Concentration

Native defects are typically responsible for generating charge carriers in Zn–Sb binary compounds. In β-Zn_4Sb_3, the hole concentration can be controlled by the amount of Zn in the system.[16,22] First-principles studies of β-Zn_4Sb_3 correspondingly suggest that the Zn vacancy is a killer defect that unyieldingly generates the p-type character of the undoped material.[23] Similar studies of native defects in ZnSb suggest that the Zn vacancy donates two holes and is the most prevalent native defect in ZnSb,[24] so it is reasonable to expect that the Zn vacancy controls the p-type conductivity in undoped ZnSb.

Table 1. Comparison of different literature studies' Seebeck coeffient and Peak zT of ZnSb. Note the Seebeck coefficients of samples with high zT correspond roughly with the Seebeck coefficient of the sample produced in phase space 4 of this study, while those with low zT have much higher Seebeck like the other phase spaces.

Author	Seebeck [μV K^{-1}] at 50 °C	Peak zT
Moghaddam et al.[21]	170	1.2
Valset et al.[7]	154	0.95
Shabaldin et al.[20]	195	0.83
Phase space 4	170 ± 10	
Böttger et al. [5]	253	0.45
Phase space 1	270 ± 10	

However, since the Zn vacancy is least likely to form in phase space 4 because it is most Zn-rich compared to the other phase spaces, the hole count generated by the Zn vacancy is expected to be lowest in this phase space. This logic is inconsistent with the experimental observation that the hole concentration is highest in phase space 4, as shown by the Hall carrier concentration in Figure 5.

The high hole concentration in phase space 4 is therefore attributed to the Sn dopant instead. Sn likely occupies the Sb site in ZnSb due to the size and chemical similarity, in which each dopant atom would then donate a hole to the system.

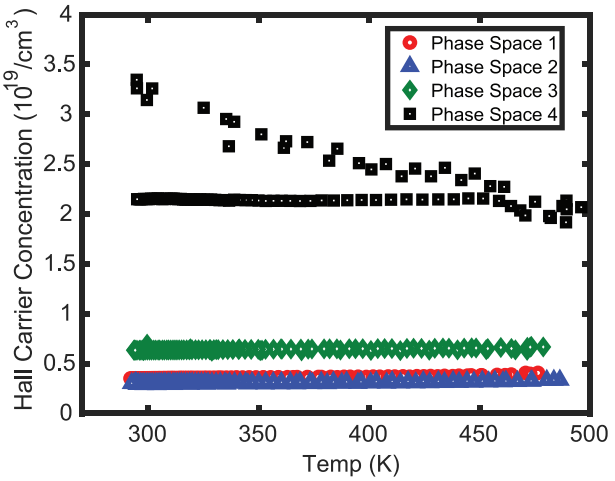

Figure 5. Hall carrier concentration as a function of temperature up to 500 K, measured for Sn-doped ZnSb samples prepared in each of the four phase spaces around the ZnSb composition in the Zn–Sb–Sn ternary phase diagram. Large hysteresis is observed in the sample synthesized in phase space 4, whereas less hysteresis is present in the other samples.

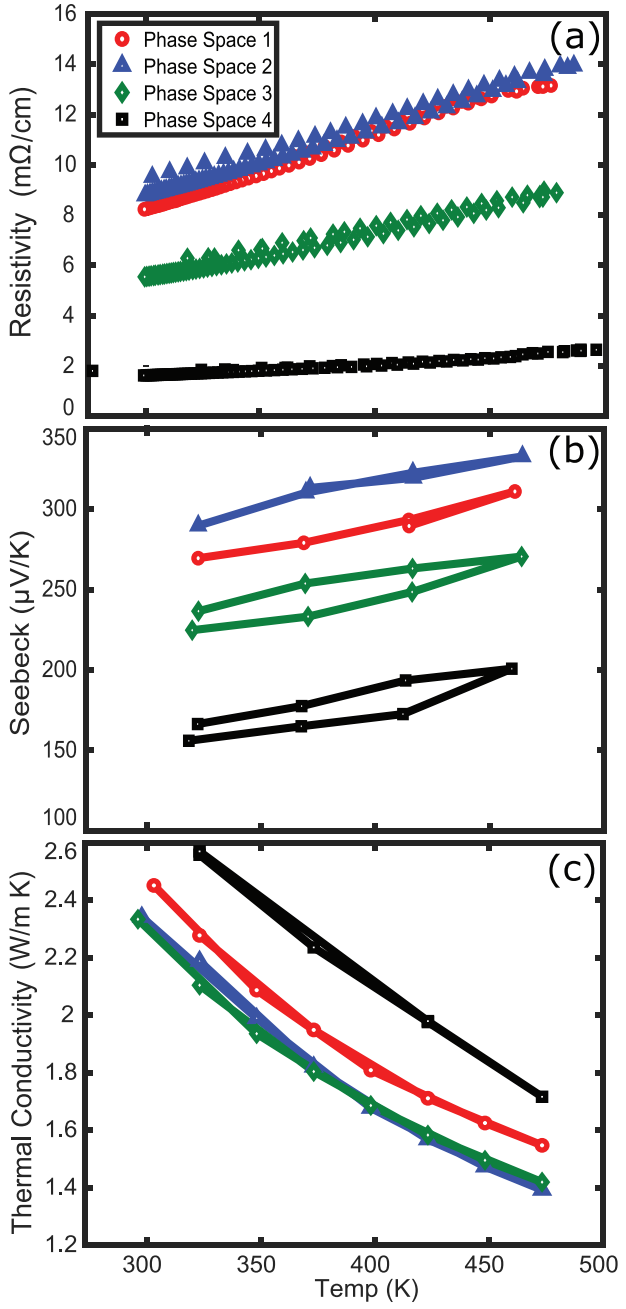

Figure 6. Thermoelectric transport properties of Sn-doped ZnSb samples prepared in phase spaces 1, 2, 3, and 4: a) the Seebeck coefficient, b) electrical resistivity, and c) thermal conductivity. Heating and cooling measurements are shown, indicating slight hysteresis.

Additionally, with the increasing amount of Sb from phase space 4 to 3 to 2 to 1, the likelihood of an Sn dopant replacing an Sb atom becomes unfavorable, which corresponds to the hole concentration decreasing in the same order.

This qualitative understanding of the dominant defect is supported by DFT calculations. The formation energy of the Sn dopant occupying an Sb site after donating a hole (denoted Sn_{Sb}^{-1}) is lower than the formation energy of the Zn vacancy after donating two holes (V_{Zn}^{-2}) near the valence band maximum under both Sb-rich and Sb-poor conditions (**Figure 8**). Since V_{Zn} is the native defect that is most likely to form in ZnSb,[24] our results suggest that the Sn dopant indeed dominates the hole concentration, especially when the sample is prepared under Sb-poor conditions.

The variation in the carrier concentrations between samples prepared in different phase regions is attributed to the position of the Fermi level under different thermodynamic conditions. By preparing the Sn-doped ZnSb samples in different three-phase regions of the Zn–Sb–Sn ternary phase diagram, we manipulate the atomic chemical potentials and, as a result, the formation energy of each defect. By changing the defect formation energies, the Fermi level shifts accordingly to achieve charge neutrality.

To illustrate for Sn_{Sb}^{-1}, the defect concentration follows a Boltzmann distribution,[25] so the charge neutrality condition for p-type ZnSb is written as

$$p^{(n)} \approx N e^{-\frac{\Delta H^{(n)}_{Sn_{Sb}^{-1}}}{kT}} \tag{2}$$

where $p^{(n)}$ and $\Delta H^{(n)}_{Sn_{Sb}^{-1}}$ are the hole concentration and the formation energy of the Sn dopant, respectively, in phase space n. The formation energy of the Sn dopant can be deduced from Equation (11) such that[26]

$$\Delta H^{(n)}_{Sn_{Sb}^{-1}} = E_{Sn_{Sb}^{-1}} - E_{Host} - \left(\mu^{\circ}_{Sn} + \Delta\mu^{(n)}_{Sn}\right) + \left(\mu^{\circ}_{Sb} + \Delta\mu^{(n)}_{Sb}\right) - E^{(n)}_{Fermi} \tag{3}$$

where the atomic chemical potentials and Fermi level explicitly depend on the phase space n. We can express the hole concentration increase, for example, from phase spaces 3 to 4 in terms of these quantities,

$$\frac{p^{(4)}}{p^{(3)}} \approx e^{\frac{\Delta H^{(3)}_{Sn_{Sb}^{-1}} - \Delta H^{(4)}_{Sn_{Sb}^{-1}}}{kT}} \tag{4}$$

and solve for the Fermi levels iteratively. The experimentally-observed carrier concentrations in phase space 3 ($p^{(3)} \approx 0.6 \times 10^{19}$ cm^{-3}) and phase space 4 ($p^{(4)} \approx 2.1 \times 10^{19}$ cm^{-3}) yield a difference in defect energy of 0.07 eV.

The observed difference in defect energy (0.07 eV) is in the range expected from estimates of the formation energies using DFT, supporting the claim that the atomic chemical potential variability in different phase spaces enables the different dopability. The calculated values for the defect energy difference from the Zn-rich to Sb-rich regions range from 0.01 to 0.54 eV depending on the assumptions used (Supporting Information). The range is large due to the uncertainty of the appropriate temperature when the defects are frozen in, the entropy and temperature dependence of the free energy of the relevant phases (some of which are liquids), the near instability of the competing crystalline phases $ZnSnSb_2$ and Zn_4Sb_3, the highly disordered Zn_4Sb_3 phase being calculated here as $Zn_{13}Sb_{10}$, the use of fitted or entirely DFT elemental reference energies, and DFT formation energy calculations in general. However, the calculated defect energy difference has the correct magnitude to suggest this thermodynamic explanation for the experimental difference in carrier concentrations.

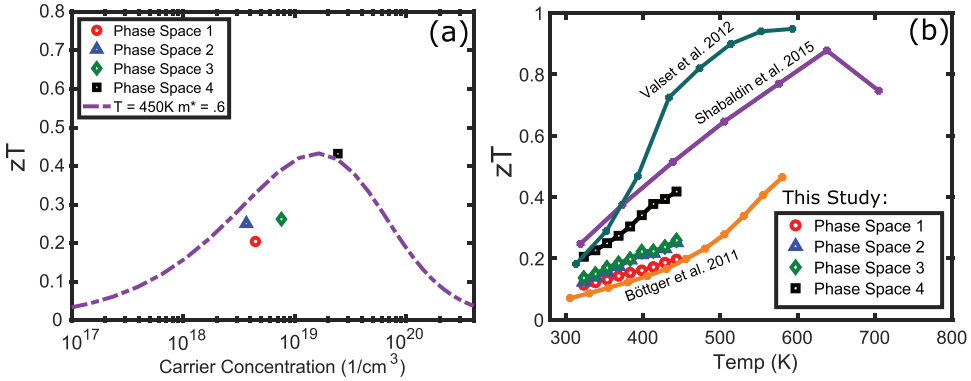

Figure 7. a) The variation of zT with carrier concentration at $T = 450$ K as expected from a model using effective mass $0.6m_e$.[5] The measured zT values of Sn-doped ZnSb samples prepared in different phase spaces are shown, in fair agreement with the expected model. b) Figure of merit zT as a function of temperature. The sample prepared in phase space 4 attains the highest zT amongst the samples prepared in this study, reaching 0.43 at 450 K. The zT is compared to previous reports of doped ZnSb samples[5,7,20] to illustrate the crucial role of phase boundary mapping in achieving optimal carrier concentration.

As an example, we show how the formation energies of ZnSb and its competing phases can be used to estimate the defect energy difference that ultimately causes the difference in hole concentration. The extrinsic atomic chemical potentials ($\Delta\mu_{Zn}^{(n)}$, $\Delta\mu_{Sb}^{(n)}$, and $\Delta\mu_{Sn}^{(n)}$) are dependent on the formation energies of the compounds constituting phase space n. For example, in phase space 3, the compounds ZnSb, $ZnSnSb_2$, and liquid Sn are in a three-phase equilibrium, which implies that the extrinsic chemical potentials are set according to the three linear equations

$$\Delta H_{Sn} = \Delta\mu_{Sn} = 0 \tag{5}$$

$$\Delta H_{ZnSb} = \frac{1}{2}(\Delta\mu_{Zn} + \Delta\mu_{Sb}) \tag{6}$$

$$\Delta H_{ZnSnSb_2} = \frac{1}{4}(\Delta\mu_{Zn} + \Delta\mu_{Sn} + 2\Delta\mu_{Sb}) \tag{7}$$

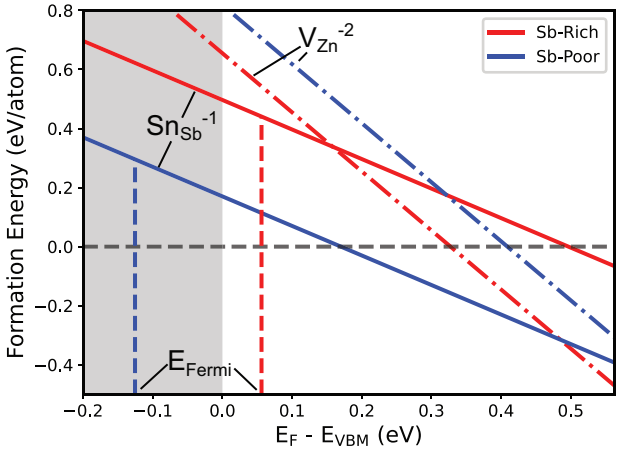

Figure 8. Defect formation energies of the Sn dopant occupying an Sb site (Sn_{Sb}^{-1}, solid) and the zinc vacancy (V_{Zn}^{-2}, dashed) under Sb-rich (red) and Sb-poor (blue) thermodynamic conditions. Sn_{Sb}^{-1} is the dominant defect near the valence band, and its formation energy is lower in the Sb-poor phase space than in the Sb-rich phase space, as expected. Consequently, the equilibrium Fermi level E_{Fermi} (dotted, vertical lines) is deeper in the valence band when the Sn-doped ZnSb sample is prepared under Sb-poor conditions.

where the formation enthalpies of each compound on the left side of each equation are given in eV per atom. We can therefore express the carrier concentration increase from phase spaces 3 to 4 as a difference in the formation enthalpies of impurity phases in the Zn–Sb–Sn phase space, where

$$\Delta\mu_{Sn}^{(3)} = \Delta\mu_{Sn}^{(4)} = 0 \tag{8}$$

$$\Delta\mu_{Sb}^{(3)} = 4\,\Delta H_{ZnSnSb_2} - 2\,\Delta H_{ZnSb} \tag{9}$$

$$\Delta\mu_{Sb}^{(4)} = \frac{1}{3}(26\,\Delta H_{ZnSb} - 23\,\Delta H_{Zn_{13}Sb_{10}}) \tag{10}$$

Consequently, the ratio of the hole concentration in different phase spaces depends on the formation enthalpies of the compounds constituting the three-phase equilibrium of the phase spaces. A similar algebra underlies the phase boundary mapping concept and has been applied to other doped systems.[8,11,12]

4. Conclusion

The thermoelectric properties of Sn-doped ZnSb are studied in four distinct phase spaces in the Zn–Sb–Sn ternary phase diagram through phase boundary mapping. It is seen that the most Zn-rich, Sb-poor phase space exhibits the highest hole carrier concentration of $\approx 2 \times 10^{19}$ cm^{-3}. By matching the observed carrier concentration to the zT expected from the single parabolic band model, we conclude that sample preparation in different phase spaces is the primary reason for the discrepancy in zT values obtained by previous reports. Density functional theory calculations qualitatively suggest that the hole concentration of Sn-doped ZnSb is determined by the Sn solubility, rather than compensation from native defects. As a result, the combined approach to understand doping concentrations in semiconductors elucidates the effectiveness of phase boundary mapping as a thermodynamic route to improving thermoelectric performance.

Table 2. Nominal composition and phases observed in XRD (Figure 3) of the samples produced for this study.

Phase space no.	Nominal composition Zn, Sn, Sb (Atomic fraction)	Observed phases
1	0.478, 0.018, 0.504	ZnSb, SnSb, Sb
2	0.47, 0.033, 0.4968	ZnSb, SnSb, $ZnSnSb_2$
3	0.48, 0.03, 0.49	ZnSb, Sn, $ZnSnSb_2$
4	0.5, 0.025, 0.475	ZnSb, Sn, Zn_4Sb_3

5. Experimental Section

Synthesis: The nominal compositions of samples studied in each of the four 3-phase regions and analyzed for this paper are shown in **Table 2**. Synthesis techniques used by Wang et al.[14] were used to target the phase spaces in the phase diagrams seen in Figure 2. The starting materials were Zn (99.999%), Sb (99.9999%), and Sn (99.999%) bulk pieces all procured from Alpha Aesar. 5 g batches of each sample were nominally loaded into evacuated quartz tubes. The tubes were heated in furnaces to 300 °C and held for 24 h, then held at 800 °C for 74 h, then water quenched. The resulting ingots were ground into fine powder and densified by hot pressing at 400 °C for 1 h under a pressure of about 60 MPa in an RF rapid hot press.[27] The pressed samples were then sealed in fused quartz tubes under vacuum and annealed at 400 °C for 72 h to ensure thermodynamic homogeneity.[14] The samples were within 95% of their theoretical density and macroscopically crack-free. Samples were then polished using Si–C grinding paper of various grades to prepare for characterization processes. They are relatively stable under ambient conditions as they were left in air for about a month without losing their luster.

Characterization: Zn–Sb samples are known to be sensitive to measurements under dynamic vacuum due to the volatility of Zn. Because loss of Zn will change the thermoelectric properties, the initial thermoelectric measurements were limited to a maximum temperature of 200 °C.[16] Resistivity was measured together with the Hall coefficient using the Van der Pauw technique under a reversible magnetic field of 2 T using pressure-assisted molybdenum electrodes.[28] The Seebeck coefficient was measured using chromel-niobium thermocouples in a custom-built system.[29] Thermal diffusivity was measured using a Netzch LFA 457. Thermal conductivity was calculated using the measured density and assuming a constant Dulong-Petit heat capacity. For phase identification, powder X-ray diffraction (XRD) and combined electron dispersive spectroscopy-wavelength diffraction spectroscopy (EDS-WDS) quantitative analysis were used. EDS-WDS was performed using a Hitachi S-3400N-II SEM equipped with Oxford INCAx-act SDD EDS system and Oxford WAVE WDS system, to determine the chemical composition and identify the secondary and primary phases in the sample. The uncertainties were considered to be 5% in resistivity, 10–20% in Seebeck, and 5–10% in thermal diffusivity.[12,28,30] The combined uncertainty for zT values might be as high as 15–20%.[12]

Density Functional Theory Calculations: First principles calculations were performed using the Vienna ab-initio simulation package (VASP)[31] using the projector-augmented wave (PAW) method.[32] The generalized gradient approximation using the Perdew–Burke–Ernzerhof (PBE) functional,[33] including spin-orbit coupling effects, were employed for all first-principles calculations. The plane-wave cutoff energy was set to 500 eV.

A supercell containing 128 atoms of the ZnSb compound was created to perform defect calculations, where the formation energy was calculated using the formula

$$\Delta H_{D^q}^{(n)} = E_{D^q} - E_{\text{Host}} - \sum n_i \mu_i^{(n)} - q E_{\text{Fermi}}^{(n)} + E_{\text{Corr}} \quad (11)$$

where $\Delta H_{D^q}^{(n)}$ is the formation energy of defect D with charge state q when the sample is prepared in phase space n, E_{D^q} is the DFT-calculated total energy of the system containing the defect with its designated charge state, and E_{Host} is the calculated total energy of the system without the defect. n_i represents the integer number of atoms added ($n_i > 0$) or removed ($n_i < 0$) from the system to create the defect, and $\mu_i^{(n)} = \mu_i^\circ + \Delta\mu_i^{(n)}$ is the atomic chemical potential of element i expressed as a deviation from the reference state of the atom μ_i°, where the deviation $\Delta\mu_i^{(n)}$ is explicitly labelled by the phase space n. $E_{\text{Fermi}}^{(n)}$ is the Fermi level, which also depended on the phase space n. E_{Corr} is the energy correction accounting for finite-size effects of the DFT calculations.[26,34]

The elemental reference energies μ_i° were set to those fitted to experimental formation enthalpies,[35] yielding a DFT phase diagram that is close to the experimentally-determined phase diagram (Figure 2). Although spin-orbit coupling was included in the defect calculations, this input had little effect on the reference energies.[35] The total energy of the monoclinic α-Zn_4Sb_3 structure was calculated, which had a 13-10 stoichiometry.

The band gap of ZnSb was corrected using GW, where the final band gap was 0.52 eV. The corresponding band edge shifts were −0.003 eV for the valence band maximum and +0.337 eV for the conduction band minimum.

Supporting Information

Supporting Information is available from the Wiley Online Library or from the author.

Acknowledgements

M.W., M.Y.T., and S.D. contributed equally to this work. The authors thank Dr. Anuj Goyal for computational assistance regarding GW band edge shifts of ZnSb. The authors acknowledge the NSF DMREF award #1729487. M.Y.T. acknowledges support from the U.S. Department of Energy through the Computational Science Graduate Fellowship (DOE CSGF) under Grant Number DE-SC0020347. This research was supported in part through the computational resources and staff contributions provided for the Quest high performance computing facility at Northwestern University, which is jointly supported by the Office of the Provost, the Office for Research, and Northwestern University Information Technology. The authors acknowledge support from the NASA Science Mission Directorate's Radioisotope Power Systems Thermoelectric Technology Development program. M.W.'s research at the Jet Propulsion Laboratory was supported by an appointment to the NASA Postdoctoral Program, administered by the Universities Space Research Association under contract with the NASA. This work was performed under the following financial assistance award 70NANB19H005 from U.S. Department of Commerce, National Institute of Standards and Technology as part of the Center for Hierarchical Materials Design (CHiMaD).

Conflict of Interest

The authors declare no conflict of interest.

Data Availability Statement

The data that supports the findings of this study are available in the supplementary material of this article.

Keywords

defect calculations, dopability, phase-boundary mapping, thermoelectric, ZnSb

Received: January 18, 2021
Revised: March 4, 2021
Published online: April 14, 2021

[1] G. J. Snyder, E. S. Toberer, in *Materials for Sustainable Energy: A Collection of Peer-Reviewed Research and Review Articles From Nature Publishing Group*, World Scientific, Singapore **2011**, p. 101.
[2] X. Song, T. G. Finstad, in *Thermoelectrics for Power Generation: A Look at Trends in the Technology*, Intech Open, London, UK **2016**, p. 117.
[3] E. S. Toberer, A. F. May, G. J. Snyder, *Chem. Mater.* **2010**, *22*, 624.
[4] a) A. O. Moghaddam, A. Shokuhfar, Y. Zhang, T. Zhang, D. Cadavid, J. Arbiol, A. Cabot, *Adv. Mater. Interfaces* **2019**, *6*, 1900467; b) Y.-H. Chu, Z.-Q. Huang, Z.-R. Yang, F.-H. Lin, K.-C. Chang, R. Suriakarthick, C.-J. Liu, *J. Eur. Ceram. Soc.* **2019**, *39*, 4177.
[5] P. M. Böttger, G. S. Pomrehn, G. J. Snyder, T. G. Finstad, *Phys. Status Solidi* **2011**, *208*, 2753.
[6] a) A. A. Shabaldin, L. V. Prokof'eva, G. J. Snyder, P. P. Konstantinov, G. N. Isachenko, A. V. Asach, *J. Electron. Mater.* **2015**, *45*, 1871; b) A. A. Shabaldin, L. V. Prokof'eva, P. P. Konstantinov, A. T. Burkov, M. I. Fedorov, *Mater. Today: Proc.* **2015**, *2*, 699; c) L. V. Prokofieva, P. P. Konstantinov, A. A. Shabaldin, *Semiconductors* **2016**, *50*, 741. d) R. Pothin, R. M. Ayral, A. Berche, D. Granier, F. Rouessac, P. Jund, *Chem. Eng. J.* **2016**, *299*, 126. e) K. Valset, X. Song, T. G. Finstad, *J. Appl. Phys.* **2015**, *117*, 045709; f) Q. Guo, S. Luo, *Funct. Mater. Lett.* **2015**, *08*, 1550028; g) M. I. Fedorov, L. V. Prokofieva, Y. I. Ravich, P. P. Konstantinov, D. A. Pshenay-Severin, A. A. Shabaldin, *Semiconductors* **2014**, *48*, 432.
[7] K. Valset, P. H. M. Böttger, J. Taftø, T. G. Finstad, *J. Appl. Phys.* **2012**, *111*, 023703.
[8] J. Male, M. T. Agne, A. Goyal, S. Anand, I. T. Witting, V. Stevanović, G. J. Snyder, *Mater. Horiz.* **2019**, *6*, 1444.
[9] a) S. A. Miller, M. Dylla, S. Anand, K. Gordiz, G. J. Snyder, E. S. Toberer, *NPJ Comput. Mater.* **2018**, *4*, 71; b) A. Goyal, P. Gorai, S. Anand, E. S. Toberer, G. J. Snyder, V. Stevanović, *Chem. Mater.* **2020**, *32*, 4467.
[10] Y. Tang, R. Hanus, S.-w. Chen, G. J. Snyder, *Nat. Commun.* **2015**, *6*, 7584.
[11] S. Ohno, K. Imasato, S. Anand, H. Tamaki, S. D. Kang, P. Gorai, H. K. Sato, E. S. Toberer, T. Kanno, G. J. Snyder, *Joule* **2018**, *2*, 141.
[12] S. Ohno, U. Aydemir, M. Amsler, J.-H. Pöhls, S. Chanakian, A. Zevalkink, M. A. White, S. K. Bux, C. Wolverton, G. J. Snyder, *Adv. Funct. Mater.* **2017**, *27*, 1606361.
[13] a) C. M. Crawford, B. R. Ortiz, P. Gorai, V. Stevanovic, E. S. Toberer, *J. Mater. Chem. A* **2018**, *6*, 24175; b) P. Jood, J. P. Male, S. Anand, Y. Matsushita, Y. Takagiwa, M. G. Kanatzidis, G. J. Snyder, M. Ohta, *J. Am. Chem. Soc.* **2020**, *142*, 15464; c) X. Li, P. Yang, Y. Wang, Z. Zhang, D. Qin, W. Xue, C. Chen, Y. Huang, X. Xie, X. Wang, M. Yang, C. Wang, F. Cao, J. Sui, X. Liu, Q. Zhang, *Research (Wash D C)* **2020**, *2020*, 4630948.
[14] C. Wang, Y. Xu, S. Yang, H. Jiang, J. Li, J. Zhu, S. Yang, X. Liu, *J. Phase Equilib. Diffus.* **2015**, *36*, 350.
[15] G. S. Pomrehn, E. S. Toberer, G. J. Snyder, A. van de Walle, *Phys. Rev. B* **2011**, *83*, 094106.
[16] E. S. Toberer, P. Rauwel, S. Gariel, J. Taftø, G. J. Snyder, *J. Mater. Chem.* **2010**, *20*, 9877.
[17] A. Nomura, S. Choi, M. Ishimaru, A. Kosuga, T. Chasapis, S. Ohno, G. J. Snyder, Y. Ohishi, H. Muta, S. Yamanaka, *ACS Appl. Mater. Interfaces* **2018**, *10*, 43682.
[18] E. Chalfin, H. Lu, R. Dieckmann, *Solid State Ionics* **2007**, *178*, 447.
[19] a) D. M. Rowe, *Materials, Preparation, and Characterization in Thermoelectrics*, CRC Press, Boca Raton, FL **2017**; b) A. Zevalkink, D. M. Smiadak, J. L. Blackburn, A. J. Ferguson, M. L. Chabinyc, O. Delaire, J. Wang, K. Kovnir, J. Martin, L. T. Schelhas, T. D. Sparks, S. D. Kang, M. T. Dylla, G. J. Snyder, B. R. Ortiz, E. S. Toberer, *Applied Physics Reviews* **2018**, *5*, 021303.
[20] A. Shabaldin, L. Prokof'eva, G. Snyder, P. Konstantinov, G. Isachenko, A. Asach, *J. Electron. Mater.* **2016**, *45*, 1871.
[21] A. O. Moghaddam, A. Shokuhfar, Y. Zhang, T. Zhang, D. Cadavid, J. Arbiol, A. Cabot, *Adv. Mater. Interfaces* **2019**, *6*, 1900467.
[22] P. Rauwel, O. M. Løvvik, E. Rauwel, J. Taftø, *Acta Mater.* **2011**, *59*, 5266.
[23] A. Faghaninia, C. S. Lo, *J. Phys.: Condens. Matter* **2015**, *27*, 125502.
[24] L. Bjerg, G. K. Madsen, B. B. Iversen, *Chem. Mater.* **2012**, *24*, 2111.
[25] D. R. Gaskell, D. E. Laughlin, *Introduction to the Thermodynamics of Materials*, CRC Press, Boca Raton, FL **2017**.
[26] C. Freysoldt, B. Grabowski, T. Hickel, J. Neugebauer, G. Kresse, A. Janotti, C. G. van de Walle, *Rev. Mod. Phys.* **2014**, *86*, 253.
[27] A. D. LaLonde, T. Ikeda, G. J. Snyder, *Rev. Sci. Instrum.* **2011**, *82*, 025104.
[28] a) K. A. Borup, E. S. Toberer, L. D. Zoltan, G. Nakatsukasa, M. Errico, J.-P. Fleurial, B. B. Iversen, G. J. Snyder, *Rev. Sci. Instrum.* **2012**, *83*, 123902; b) K. A. Borup, J. de Boor, H. Wang, F. Drymiotis, F. Gascoin, X. Shi, L. Chen, M. I. Fedorov, E. Müller, B. B. Iversen, *Energy Environ. Sci.* **2015**, *8*, 423.
[29] S. Iwanaga, E. S. Toberer, A. LaLonde, G. J. Snyder, *Rev. Sci. Instrum.* **2011**, *82*, 063905.
[30] H. Wang, W. D. Porter, H. Böttner, J. König, L. Chen, S. Bai, T. M. Tritt, A. Mayolet, J. Senawiratne, C. Smith, *J. Electron. Mater.* **2013**, *42*, 654.
[31] a) G. Kresse, J. Hafner, *Phys. Rev. B* **1993**, *47*, 558; b) G. Kresse, J. Furthmüller, *Comput. Mater. Sci.* **1996**, *6*, 15; c G. Kresse, J. Furthmüller, *Phys. Rev. B* **1996**, *54*, 11169.
[32] a) P. E. Blöchl, *Phys. Rev. B* **1994**, *50*, 17953; b) G. Kresse, D. Joubert, *Phys. Rev. B* **1999**, *59*, 1758.
[33] J. P. Perdew, K. Burke, M. Ernzerhof, *Phys. Rev. Lett.* **1996**, *77*, 3865.
[34] C. Freysoldt, J. Neugebauer, C. G. van de Walle, *Phys. Rev. Lett.* **2009**, *102*, 016402.
[35] V. Stevanović, S. Lany, X. Zhang, A. Zunger, *Phys. Rev. B* **2012**, *85*, 115104.